Spin-orbit driven ferromagnetic resonance

D. Fang, H. Kurebayashi, J. Wunderlich, K. Výborný, L. P. Zârbo,
R. P. Campion, A. Casiraghi, B. L. Gallagher, T. Jungwirth & A. J. Ferguson

I. DERIVATION OF FMR LINESHAPE AND ITS ANGLE DEPENDENCE

The total voltage across the device is given by Ohm's law:

$$V(t) = I(t) \cdot R(t) \tag{S1}$$

Here $I(t) = I\cos(\omega t)$ is an ac current within the sample. Next we look at the time-dependent resistance $R(t)$. In general, the anisotropic magnetoresistance (AMR) describes the change in the sample's longitudinal resistance when its magnetisation $\mathbf{M}$ forms an angle θ with respect to the current $\mathbf{I}$ [1]:

$$R(t) = R_\perp - \Delta R \cos^2\theta(t) \tag{S2}$$

where $R_\perp$ is the longitudinal resistance when $\mathbf{M} \perp \mathbf{I}$ and $\Delta R = R_\perp - R_\parallel$ is the AMR coefficient ($R_\parallel$ is the longitudinal resistance for $\mathbf{M} \parallel \mathbf{I}$). In our samples, we measure $\Delta R > 0$ (and $\Delta R/R_\perp$ of the order of few per cent) as it is commonly the case in (Ga,Mn)As epilayers; we note that Eq. (S2) neglects the crystalline contributions to the AMR [1] that we confirmed to be small in magnitude.

In our experiment, the magnetic moments in the micro-bar are precessing driven by an ac current-induced torque, resulting in a time-varying angle:

$$\theta(t) = \theta + \theta_c \cos(\omega t - \psi) \tag{S3}$$

where θ_c describes the deviation of $\mathbf{M}$ from its axis of rotation (referred to as the 'cone angle' of the precession), and ψ is the phase difference between the resistance and the ac current. An expression for the time-varying resistance $R(t)$ can thus be obtained by combing Eq. (S2) and (S3). In the case of small cone angle precession, the expression can be simplified by expanding $\cos^2\theta(t)$ up to first order:

$$R(t) \approx R_\perp - \Delta R \left[\cos^2\theta - 2\theta_c \cos\theta \sin\theta \cos(\omega t - \psi)\right] \tag{S4}$$

Combining Eq. (S1) and (S4), we see that the total voltage $V(t)$ comprises terms at frequencies ω and 2ω, and a time-independent (dc) term V_{dc}, which is the focus of this derivation.

To find out the expression for θ_c, we need to determine the magnetisation components in the plane of rotation. We define the geometry for our experiment in Figure S1. Since the applied dc magnetic field $\mu_0\mathbf{H}_0$ is much larger than the anisotropy of the ferromagnet (measured to be a few tens of mT), the magnetisation vector $\mathbf{M}$ stays parallel to $\mathbf{H}_0$. A second coordinate system $x' - y'$ is defined with respect to $\mathbf{M}$. In the new coordinates, $\mathbf{H}_0 = (H_0, 0, 0)$, and $\mathbf{M} = (M_s, m_{y'}e^{i\omega t}, m_z e^{i\omega t})$ in the case of small angle precession.

The dynamics of the damped magnetic motion is described phenomenologically by the Landau-Lifshitz-Gilbert (LLG) equation:

$$\frac{\partial \mathbf{M}}{\partial t} = -\gamma \mathbf{M} \times (\mathbf{H}_{\text{tot}} + \mathbf{h}_{\text{eff}}) + \frac{\alpha}{M_s}\left(\mathbf{M} \times \frac{\partial \mathbf{M}}{\partial t}\right) \tag{S5}$$
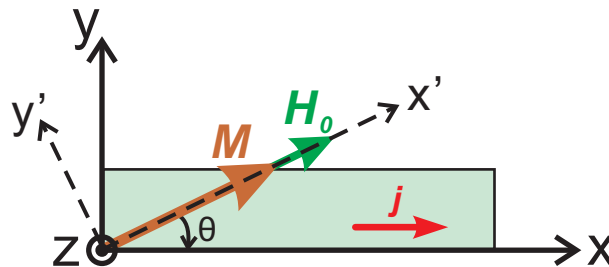

FIG. S1: The coordinate systems used in the derivation.

here the first term is the field torque and the second term is the Gilbert damping. This process is illustrated in Figure 1a in the text. γ is the gyromagnetic ratio and α is the phenomenological Gilbert damping constant. $\mathbf{H}_{\text{tot}}$ is the total magnetic field in the vicinity of the magnetisation. It is a vector sum of the dc magnetic field $\mathbf{H}_0$, the demagnetisation field $\mathbf{H}_{\text{demag}}$ and the anisotropy of the material $\mathbf{H}_{\text{ani}}$. $\mathbf{h}_{\text{eff}}$ is the microwave frequency effective magnetic field which drives the magnetic moments (resulting from SO-coupling and exchange interaction); in the $x' - y'$ system, it has the form:

$$\mathbf{h}_{\text{eff}} = \begin{pmatrix} h_x \cos\theta - h_y \sin\theta \\ h_x \sin\theta + h_y \cos\theta \\ h_z \end{pmatrix} e^{i\omega t} \tag{S6}$$

Solving Eq. (S5) and discarding high-order terms, we obtain the following set of linearised equations [2]:

$$\frac{i\omega}{\gamma}m_{y'} + \left(\frac{i\alpha\omega}{\gamma} + H_0 + H_1\right)m_z = M_s h_z \tag{S7}$$

$$\left(\frac{i\alpha\omega}{\gamma} + H_0 + H_2\right)m_{y'} - \frac{i\omega}{\gamma}m_z = M_s(h_x\sin\theta + h_y\cos\theta) \tag{S8}$$

where

$$H_1 = M_s - H_{2\perp} + H_{2\|}\cos^2\left(\varphi + \frac{\pi}{4}\right) + \frac{1}{4}H_{4\|}(3 + \cos 4\varphi) \tag{S9}$$

$$H_2 = H_{4\|}\cos 4\varphi - H_{2\|}\sin 2\varphi \tag{S10}$$

are terms containing the demagnetisation and anisotropy fields of the (Ga,Mn)As epilayers. Here $H_{2\perp}$, $H_{2\|}$ and $H_{4\|}$ represent the out-of-plane uniaxial, in-plane uniaxial and in-plane biaxial anisotropy, respectively. They are related to the energy terms K_i according to $H_i = 2K_i/\mu_0 M_s$. φ is the angle between the magnetisation vector $\mathbf{M}$ and the [100] crystallographic axis.

In (Ga,Mn)As epilayers, due to the strong in-plane anisotropy, the precessional motion of the magnetisation is highly elliptical, with the maximum deviation from its equilibrium position for $\mathbf{M}$ in-plane with the sample. For small angle precession, the cone angle is $\theta_c = m_{y'}/M_s$. Note that the out-of-plane component of the precession leads to a sinusoidal change in resistance at 2ω [3]. Therefore this term doesn't contribute a DC voltage when mixed with the oscillatory current at ω, so only the in-plane component (θ_c) of the elliptical precession is used in our derivation. Its value can be obtained by solving Eq. (S7) and (S8):

$$\theta_c = -\frac{ih_z\gamma}{\omega} - \frac{[i(H_0 + H_1) - \Delta H]\left[\gamma h_z(H_0 + H_2 + i\Delta H) - i\omega(h_x\sin\theta + h_y\cos\theta)\right]}{\omega\left[-(H_0 + H_1 + i\Delta H)(H_0 + H_2 + i\Delta H) + \omega^2/\gamma^2\right]} \tag{S11}$$

Here $\Delta H = \alpha\omega/\gamma$ defines the resonance linewidth (half width at half maximum). The complex expression of Eq. (S11) arises from the complex susceptibility.

Combining Eq. (S1), (S4) and (S11), a general expression for the *dc* voltage is obtained:

$$V_{\text{dc}} = -\frac{1}{2}I\Delta R\sin(2\theta) \left\{ \frac{i\gamma h_z}{\omega} + \frac{1}{\omega\left[-(H_0 + H_1 + i\Delta H)(H_0 + H_2 + i\Delta H) + \omega^2/\gamma^2\right]} \right.$$
$$\left[i(H_0 + H_1) - \Delta H\right]\left[\gamma h_z(H_0 + H_2 + i\Delta H)\right.$$
$$\left. \left. -i\omega(h_x\sin\theta + h_y\cos\theta)\right] \right\} \tag{S12}$$

In conventional FMR experiments, the frequency of the driving field ω is kept constant, and the external field $\mathbf{H}_0$ is swept. To determine the lineshape of the dc voltage near resonance, we consider the profile of V_{dc} at a small deviation δH from H_{res}, i.e.

$$\delta H = |H_0 - H_{\text{res}}| \tag{S13}$$

For uniform precession of $\mathbf{M}$ in a material with small damping ($\alpha \ll 1$), $\Delta H \ll H_{\text{res}}$. Also since we only consider small perturbations near the resonance, $\delta H \ll H_{\text{res}}$. Substituting Eq. (S13) into (S12) and only keeping terms linear
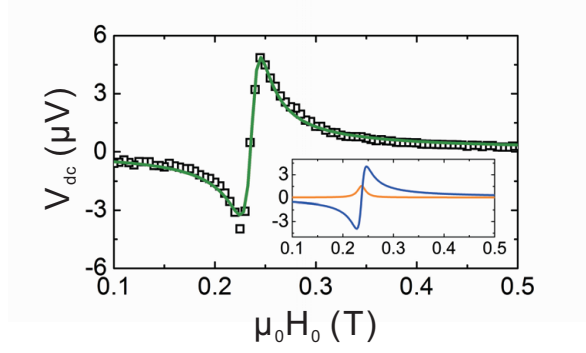
FIG. S2: The magnetic resonance is reflected in the dc voltage measured across a device. Inset: the two Lorentzian components of the resonance peak.

in δH and ΔH, the following simplified expression is obtained:

$$V_{\mathrm{dc}} = -\frac{1}{2}I\Delta R\sin(2\theta)\left\{\frac{i\gamma h_z}{\omega} - \frac{1}{\omega(2H_{res}+H_1+H_2)(\delta H+i\Delta H)}\right.$$

$$\left[\omega(h_x\sin\theta+h_y\cos\theta)(\delta H+H_{res}+H_1+i\Delta H)+\right.$$

$$\gamma h_z\Big(i\delta H(2H_{res}+H_1+H_2)+i(H_{res}+H_1)(H_{res}+H_2)-$$

$$\left.\left.\Delta H(2H_{res}+H_1+H_2)\Big)\right]\right\} \tag{S14}$$

The in-phase (real) component of V_{dc} has the form (keeping only terms linear in α):

$$\mathrm{Re}\{V_{\mathrm{dc}}\} = V_{\mathrm{sym}}\frac{\Delta H^2}{(H_0-H_{\mathrm{res}})^2+\Delta H^2} + V_{\mathrm{asy}}\frac{\Delta H(H_0-\Delta H)}{(H_0-H_{\mathrm{res}})^2+\Delta H^2} \tag{S15}$$

with angle-dependent amplitudes

$$V_{\mathrm{sym}}(\theta) = \frac{I\Delta R}{2}A_{\mathrm{sym}}\sin(2\theta)h_z \tag{S16}$$

$$V_{\mathrm{asy}}(\theta) = \frac{I\Delta R}{2}A_{\mathrm{asy}}\sin(2\theta)(h_x\sin\theta+h_y\cos\theta) \tag{S17}$$

Eq. (S15) shows that the FMR peak is a combination of symmetric and anti-symmetric Lorentzian functions, as illustrated in Figure S2. The symmetric Lorentzian function is caused by an out-of-plane driving field h_z; whereas the anti-symmetric Lorentzian results from in-plane driving fields h_x & h_y, and its amplitude depends on the relative orientation of the driving field with respect to the current. The terms A_{sym} and A_{asy} are the scalar amplitudes of the magnetic susceptibility ($A_i = \chi_i/M_s$):

$$A_{\mathrm{sym}} = \frac{\gamma(H_{\mathrm{res}}+H_1)(H_{\mathrm{res}}+H_2)}{\omega\Delta H(2H_{\mathrm{res}}+H_1+H_2)} \tag{S18}$$

$$A_{\mathrm{asy}} = \frac{(H_{\mathrm{res}}+H_1)}{\Delta H(2H_{\mathrm{res}}+H_1+H_2)} \tag{S19}$$

We notice that the saturation magnetisation M_s does not enter the expression of V_{dc} explicitly. This is a major convenience as M_s cannot be deduced from FMR experiments, and other measurements such as SQUID and VSM are required to determined its value. The terms A_{sym} and A_{asy} are also angle-dependent, since they depend on the magnetic anisotropy of the device.

On the other hand, the 90º out-of-phase (imaginary) component of V_{dc} consists of two Lorentzians with the following
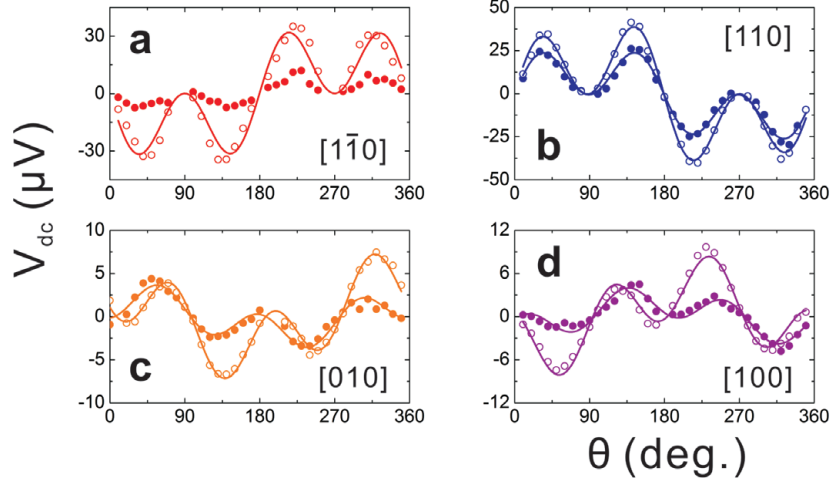
FIG. S3: Amplitudes of the symmetric and anti-symmetric Lorentzian parts $V_{\mathrm{sym}}(\theta)$ and $V_{\mathrm{asy}}(\theta)$ measured on a group of 500 nm-wide (Ga,Mn)As bars (solid and hollow circles, respectively), patterned along different crystalline directions. The solid lines are fitted results to Eq. (S17).

amplitudes:

$$V'_{\mathrm{sym}}(\theta) \;=\; -\frac{I\Delta R}{2}A_{\mathrm{asy}}\sin(2\theta)(h_x\sin\theta + h_y\cos\theta) \tag{S20}$$

$$V'_{\mathrm{asy}}(\theta) \;=\; \frac{I\Delta R}{2}A_{\mathrm{sym}}\sin(2\theta)h_z \tag{S21}$$

This implies that if there is any phase difference between the current and the oscillating resistance, the angular dependence of V_{asy} is partially mapped onto V_{sym} and vice versa.

The anti-symmetric Lorentzian contribution is dominant but a symmetric Lorentzian contribution is present in our measurement (Figure S3), of which the θ-dependence can also be described with a combination of $\sin 2\theta\cos\theta$ and $\sin 2\theta\sin\theta$ functions, instead of a $\sin 2\theta$ curve. This indicates that the V_{sym} in our measurement is not caused by an out-of-plane driving field but rather by a phase-shift between the driving field and the current. The magnitude of V_{sym} varies among devices patterned in different crystal directions, and this systematic trend has been observed among many different devices of different sizes. To evaluate the magnitude of the driving fields we consistently fit to the larger anti-symmetric Lorentzian line.

II. DEDUCING THE CURRENT-INDUCED EFFECTIVE FIELD

Rearranging Eq. (S17) gives the following expression:

$$\frac{2V_{\mathrm{asy}}(\theta)}{I\Delta RA_{\mathrm{asy}}(\theta)} = h_x\sin 2\theta\sin\theta + h_y\sin 2\theta\cos\theta \tag{S22}$$

This implies that for a micro-bar patterned along either [100] or [010] direction, the excitation field due to Dresselhaus and Rashba spin-orbit interaction can be separately determined (as shown in Figure 3c and 3d in the main text). In the case of [110]/[1$\bar{1}$0] bars, the two fields are collinear and cannot be directly deduced from Eq. (S22). Notice also that both V_{asy} and A_{asy} are angle-dependent terms.

To calculate the magnetic fields, we measure the amplitude of the FMR peak at $\theta = 55^\circ$ and 305°. The anti-symmetric Lorentzian then becomes:

$$\frac{2V_{\mathrm{asy}}(55^\circ)}{I\Delta RA_{\mathrm{asy}}(55^\circ)} \;=\; 0.77h_x + 0.54h_y \tag{S23}$$

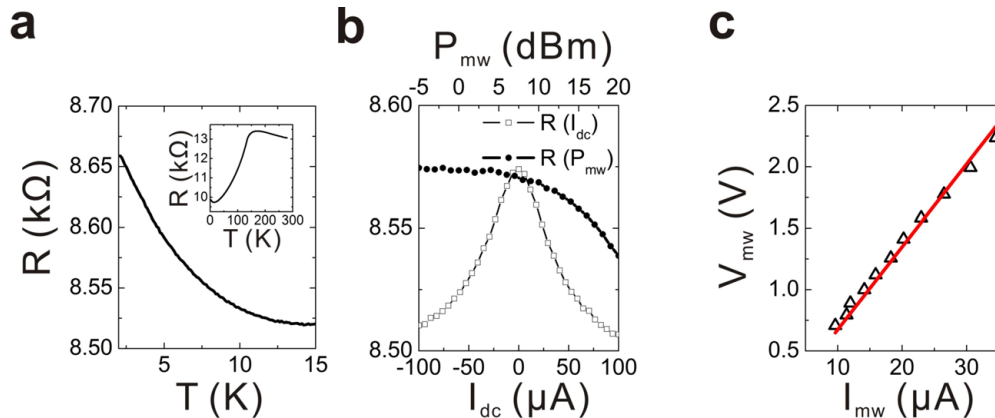$$\frac{2V_{\mathrm{asy}}(305^\circ)}{I\Delta RA_{\mathrm{asy}}(305^\circ)} \;=\; 0.77h_x - 0.54h_y \tag{S24}$$

FIG. S4: Determination of the microwave current using Joule heating. **a,** The temperature dependence of a device's longitudinal resistance $R(T)$, in the temperature range where the experiments are carried out (6 K). Inset: The sample resistance measured over the entire temperature range 2.5 – 270 K. **b,** The change in sample resistance caused by Joule heating from both a direct current $R(I_{dc})$ and the microwave power $R(P_{mw})$ (P is the value shown on the signal generator). **c,** The calibrated I_{mw}-V_{mw} curve (triangles), where V_{mw} is the rms voltage output into the 50 Ω transmission line. The calibration errors are smaller than the size of the triangles in the graph (~ 0.3 μA), and they are caused by uncertainties in finding the exact value of the microwave current with respect to the direct current.

Here V_{asy} is determined from fittings to the FMR peak; the longitudinal AMR coefficient ΔR can be determined from transport measurements; and A_{asy} are calculated using Eq. (S19) and the magnetic anisotropy of the device. The amplitude of the microwave current $I \cos \omega t$ can be calibrated by comparing the Joule heating from a known direct current and the microwave current (see Figure S4). Then by adding and subtracting Eq. (S23) and (S24), we are able to separately calculate the magnitude of the in-plane driving field along the bar (h_x) and perpendicular to the bar (h_y), which arise from the Dresselhaus and Rashba spin-orbit interaction, respectively.

In order to find out the current density dependence of the driving fields (as shown in Figure 3e and 3f in the main text), the above measurement is repeated for different microwave power P.

III.   CALIBRATION OF MICROWAVE CURRENT

In order to determine the microwave current we use the Joule heating of the sample as a calibration. This is possible because of the strong temperature dependence of the sample resistance (Figure S4a). The resulting change in sample resistance is measured both from the Joule heating of a direct current and also the incident microwave signal (Figure S4b). By comparing these two quantities we infer the microwave current through the sample. We perform this calibration for a wide range of microwave powers. An example is shown in figure S4c where, as expected, a linear relationship is observed between the inferred microwave current and the voltage at the microwave source.

Does the microwave power from the heating estimate make sense given the expected microwave power at the sample? The semi-rigid coaxial cables are UT85-B-SS, and neither the CuBe core nor the stainless steel jacket dramatically change resistance (and therefore microwave attenuation) between RT at 4 K (the attenuation for similar cables decreases by about 20% on cooling). Therefore, a room temperature measurement with a diode detector allows us to estimate the power reaching the sample.

At a source power 100 mW ($f = 17$ GHz), the microwave power reaching the sample is 2.8 mW, which corresponds to a microwave voltage of 0.74 V. Here, it is assumed that there is a standing wave voltage of twice the incident voltage due to the nearly open circuit presented by the nano-bar. This voltage, when divided by the 500 nm sample resistance (17 kΩ), gives us an expected microwave current at 44 μA, close to the value obtained using Joule heating (33 μA). Note this measurement doesn't account for the additional loss on the PCB and in the bond-wire to the actual sample.

Due to the high-impedance of the sample, it is relevant to ask if the microwave current dissipates power only in the contact region or also in the bar itself. We first perform a measurement of the dc contact resistance of the sample. A set of bars of different lengths were measured and the resistance determined as a function of length. This yields a contact resistance ($2R_c$) where R_c=0.8 kΩ.

In the contact region the current prefers to flow in the lower resistivity metal rather than in the doped semiconductor.

Let's conservatively estimate that the contact is effectively made to the semiconductor at 25 μm from the 500 nm × 10 μm device. Thus all device lengths are small with respect to the wavelength of signal (l$\sim$500 μm, assuming wavelength (at 17 GHz) reduced by the dielectric constant of GaAs). Therefore, Kirchoff's laws can be applied, and we see that the total instantaneous current is the same in contact region and the device. As a result the power dissipation is $I^2 R_c$ in the source contact region and $I^2 R$ in the device. Since $R \gg R_c$ we can see that the majority of the power gets dissipated in the device itself and not the contact region.

IV. DEMAGNETISING FIELD CONTRIBUTION TO MAGNETIC ANISOTROPY

We first notice that due to the relatively low saturation magnetisation of the diluted magnetic semi-conductor the shape anisotropy is small compared to the crystalline anisotropies. Below we have cal-culated the demagnetisation factors and the corresponding shape anisotropies for the different bars investigated. The demagnetisation field along the bar (x-direction) is negligible due to the long sample extension compared to the layer thickness and bar width, respectively. The calculated de-magnetising factors and the corresponding shape anisotropies are listed in the following table [4].

Bar width	D_Z (perp. to plane)	D_Y (inplane, perp. to bar)	shape anisotropy energy [kJ/m^3] $0.5\ \mu_0\ D_{Z/Y}\ M_S^2$ ($M_S/\mu_0 = 60$ mT)
80 nm	0.83	0.17	1.19 / 0.24
500 nm	0.96	0.04	1.37 / 0.06
4 μ m	0.99	0.01	1.42 / 0.01
2D plate	1	0	1.43 / 0.00

The in plane demagnetising field perpendicular to the bar-orientation is insignificant when considering the relatively small magnetic layer thickness and the relatively larger magnitude of the crystalline anisotropy fields. Any contribution from this demagnetising field has the same symmetry as the anisotropy field due to strain relaxation. We note that there is a small contribution to the observed H_U only in the 80nm bar due to the demagnetising field. For the other samples it is sufficient to incorporate the shape anisotropy of an infinitely extended thin film when modelling the FMR conditions of our samples.

V. DRIVING FIELD HOMOGENEITY

We discuss the uniformity of the excitation field. The effect of non-uniform excitation on FMR spectra has previously been examined [5]. A gradient of the excitation field was created across a NiFe sample and the effect on FMR lineshape investigated. It was found that long wavelength spin-wave excitations, with k-vectors along the excitation gradient, modified the FMR lineshape. In our case, any non-uniformity in current density will lead to a non-uniform driving field.

We expect that the largest current density asymmetry lies in the z-direction. This potentially leads to excitation of spin-waves with k-vectors in the z-direction (surface spin-wave mode). Discrete resonances due to the spin-waves have previously been observed in (Ga,Mn)As [6], however we have not to date observed the resulting spectra in our experiments. The current density may also vary along the y-direction due to the carrier depletion and/or modified scattering rates at the sample edges. Based on the measurements cited above, the spin-wave pattern should be resolvable in the 500 nm and 80 nm bars, but we observe no such resonance. So we conclude that any driving field inhomogeneity that is present doesn't significantly affect our FMR spectroscopy.

VI. OERSTED FIELD

For a symmetric current distribution within the wire there should be no rectification effect since the time-varying magnetic field averages to zero. However, it was shown for a metallic wire [7, 8] that the current distribution in a real wire need not be symmetric due to different reflection coefficients from the top and bottom interfaces or due to the asymmetry between the dielectrics on top and beneath the wire. Similar considerations apply to our semiconducting case. The resulting field from an asymmetric current distribution is in-plane with the wire and perpendicular to the
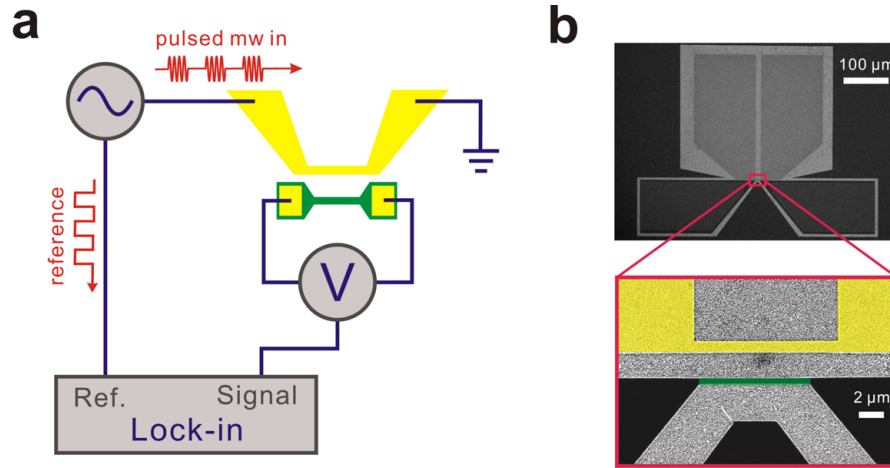
FIG. S5: FMR on individual submicron devices using on-chip generated driving field. **a,** Schematic of the experimental setup, which utilises a current-carrying waveguide to generate a local excitation field to drive magnetisation precession. Signal detection is achieved using the frequency mixing effect, and the lock-in technique is also employed to increase the measurement sensitivity. **b,** SEM images of the device, which consists of a shorted coplanar stripline waveguide (yellow false colour) and a 500 nm-wide (Ga,Mn)As micro-bar (green false colour). The waveguide is patterned on an area where the (Ga,Mn)As epilayer has been chemically removed, leaving only the semi-insulating GaAs substrate.

current direction. As such it would directly contribute to our measurement of $\mathbf{h}_R$, but not to $\mathbf{h}_D$, in the [100] and [010] bars. From the data we cannot precisely determine the Oersted contribution to h_R. However, we make the following observations which indicate that $\mathbf{h}_R$ is largely dependent on the material properties.

The measured value of $\mathbf{h}_R$ changes sign between the (Ga,Mn)As and (Ga,Mn)(As,P) material, indicating that it depends on the material properties and not just a current distribution. A shift in the sign of the crystalline uniaxial anisotropy, parameterised by an effective strain e_{xy}, occurs between these materials showing agreement with the theoretical model.

An Ampere's law estimate gives a field of 60 μT at the surface of the 500 nm bars at a current density of 2×10^5 Acm^{-2}. This provides an upper limit to the size of the Oersted field that could be measured, with its contribution to $\mathbf{h}_R$ depending on the current profile and likely to be several orders of magnitude less. For comparison, in the metallic case, where much higher current densities of 6×10^6 Acm^{-2} were used, the field at the surface was estimated to be 1.5 mT, leading to a calculated $\mathbf{h}_R$ (h_y in their notation) field of 5 μT [7, 8]. In our case the current density is at least an order of magnitude smaller, so for the same current asymmetry as in the metallic case, the contribution to $\mathbf{h}_R$ would be smaller that 1 μT i.e. significantly smaller than the measured signal.

VII. COMPARISON BETWEEN SO-FMR AND CONVENTIONAL WAVEGUIDE-DRIVEN FMR

In this Section, FMR results from 500 nm-wide (Ga,Mn)As bars using two different techniques are compared: One device is measured using SO-FMR; while the other one is measured using a more conventional on-chip FMR technique, which has been employed previously on metal systems [7, 9, 10].

Using the latter technique, illustrated in Figure S5, the magnetisation is driven by a local microwave magnetic field, generated by a coplanar stripline waveguide (CPS) lithographically defined next to the device. The microwave field is out-of-plane. This field also induces a microwave current $I \cos \omega t$ inside sample, allowing us to detect the magnetic motion via the AMR frequency mixing effect.

The experimental results using the two very different techniques are compared in Figure S6. The resonance peaks from both experiments can be seen in Figures S6a and S6d. According to Eq. (S15), we expect that the FMR signal, reflected in the dc voltage spectrum, should possess a predominant symmetric Lorentzian lineshape if the magnetic motion is driven by an out-of-plane field; whereas it should be an anti-symmetric Lorentzian curve when driven by an in-plane excitation field (such as the current-induced field). This is indeed observed in our measurements.

The frequency-dependence of the resonance field H_{res} can be well-described with the equation of ferromagnetic resonance $\omega^2 = \gamma^2 \mu_0^2 (H_{\text{res}} + H'_{\text{ani}})(H_{\text{res}} + H''_{\text{ani}})$ in both cases, as demonstrated in Figures S6b and S6e.

The frequency-dependence of the FMR linewidth ΔH can also be determined, and the Gilbert damping constants are found to be $\alpha = 0.04$ for the device with 3% Mn and $\alpha = 0.009$ for the device with 6% Mn. This is understandable
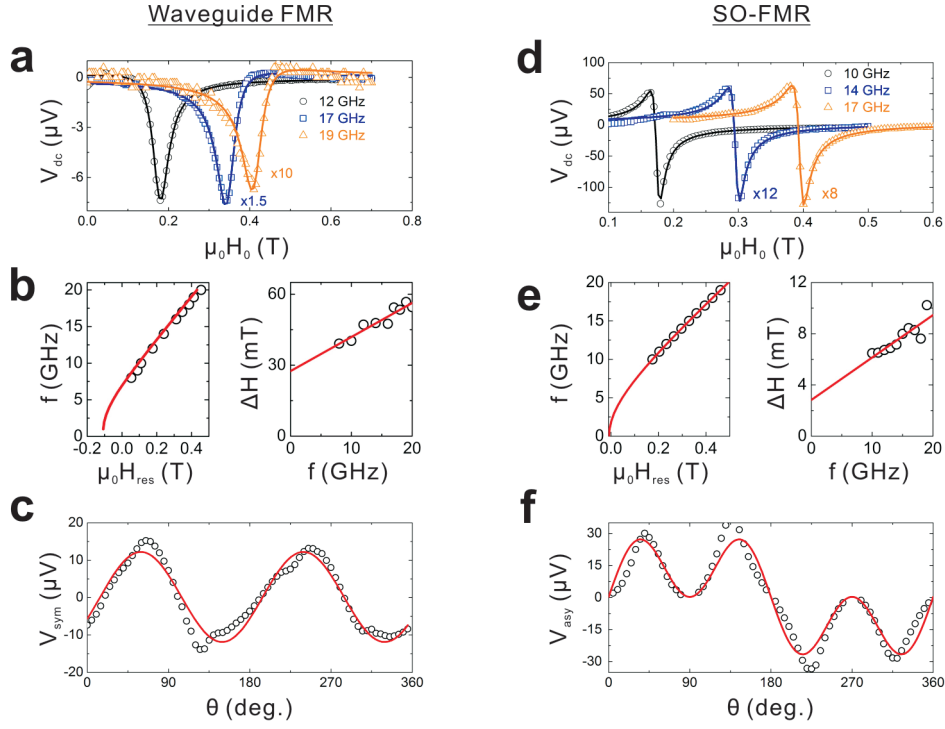
FIG. S6: Comparison between the two types of FMR experiments. **a − c,** Ferromagnetic resonance observed on a 500 nm-wide bar (3% Mn) driven by a real microwave magnetic field generated with a current-carrying waveguide. The plots show FMR peaks observed at different driving frequencies, frequency-dependence of $H_{\rm res}$ and ΔH, and the θ-dependence of the FMR amplitude $V_{\rm sym}$. The solid lines in each graph are fittings. **d − f,** Ferromagnetic resonance observed on a 500 nm-wide bar (6% Mn) driven by the current-induced effective field.

as the damping scales inversely with the hole concentration.

Finally, the θ-dependence of the dc voltage amplitude are compared. For the sample with a waveguide, Figure S6c shows that the amplitude of the symmetric Lorentzian $V_{\rm sym}$ can be described by a $\sin 2\theta$ function, which according to Eq. (S16), is the characteristic of an out-of-plane driving field $\mathbf{h}_{\rm mw}(t) = (0, 0, h_z)e^{i\omega t}$. This agrees with the expected driving field direction and serves to confirm our vector magnetometry. For the sample ([110] bar) measured with SO-FMR, its anti-symmetric Lorentzian amplitude $V_{\rm asy}$ exhibits $\sin 2\theta \cos \theta$ behaviour, consistent with a driving field $\mathbf{h}_{\rm eff}(t) = (0, h_y, 0)e^{i\omega t}$.

We also evaluate the two methods in terms of their ability to detect the magnetic anisotropy. Figure S7 compares the anisotropy measured in two (Ga,Mn)As bars of identical size (500 nm-wide, 10 μm-long) using the two different techniques. In the conventionally driven sample (Figure S7a), away from the end of the waveguide, the field drops more slowly ($\sim a/r + b/r^2$) leading to some FMR signals in the contacts. As a result, the contribution from the contact regions makes the local changes in the anisotropy of the device difficult to determine. By contrast, in SO-FMR since the driving field is proportional to the current density, which drops rapidly in the contact region, FMR is almost localised to the bar, and the change in anisotropy due to strain relaxation is clearly observed (Figure S7b).

VIII. THEORETICAL MODEL

Microscopically, $\mathbf{h}_{\rm D}$ and $\mathbf{h}_{\rm R}$ can be linked to the term $\mathcal{H}_{\rm C4}$ in the effective Hamiltonian describing (Ga,Mn)As [11–15]:

$$\mathcal{H} = \mathcal{H}_{\rm KL} + \mathcal{H}_{\rm exch} + \mathcal{H}_{\rm C4} \tag{S25}$$

Here $\mathcal{H}_{\rm KL}$ is the inversion symmetric part of the host GaAs semiconductor Hamiltonian, $\mathcal{H}_{\rm exch}$ describes the exchange interaction between carrier (hole) spins and local moments (of Mn), and the $\mathcal{H}_{\rm C4}$ term is due to broken inversion symmetry and the presence of strain (e_{ij}).
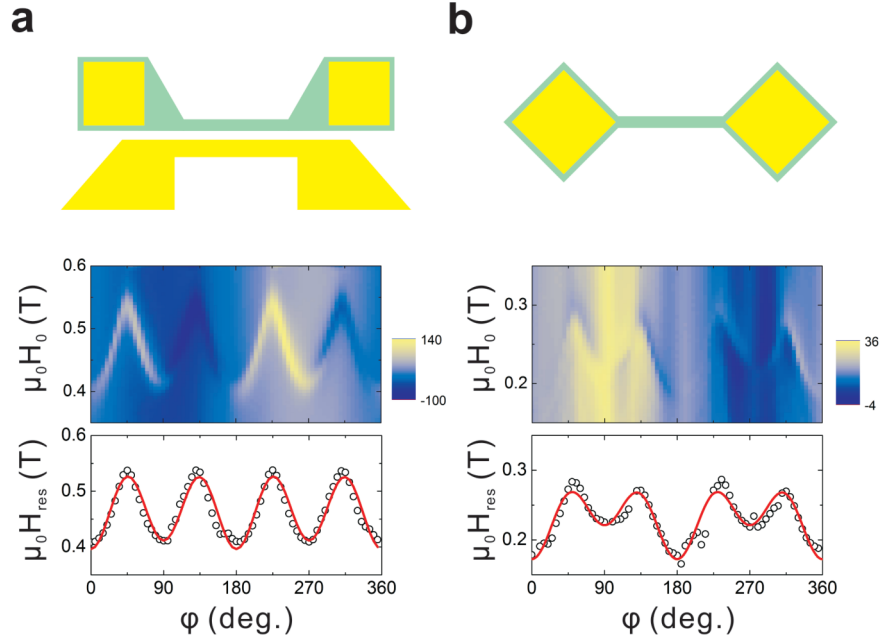
FIG. S7: Comparison of the magnetic anisotropy measured using the two types of FMR techniques. **a,** Magnetic anisotropy measured on a 500 nm-wide bar (6% Mn, unannealed) using the conventional waveguide FMR technique. The sample geometry is schematically illustrated in the top graph. **b,** Anisotropy measured on a 500 nm-wide bar (6% Mn, unannealed) using the SO-FMR setup.
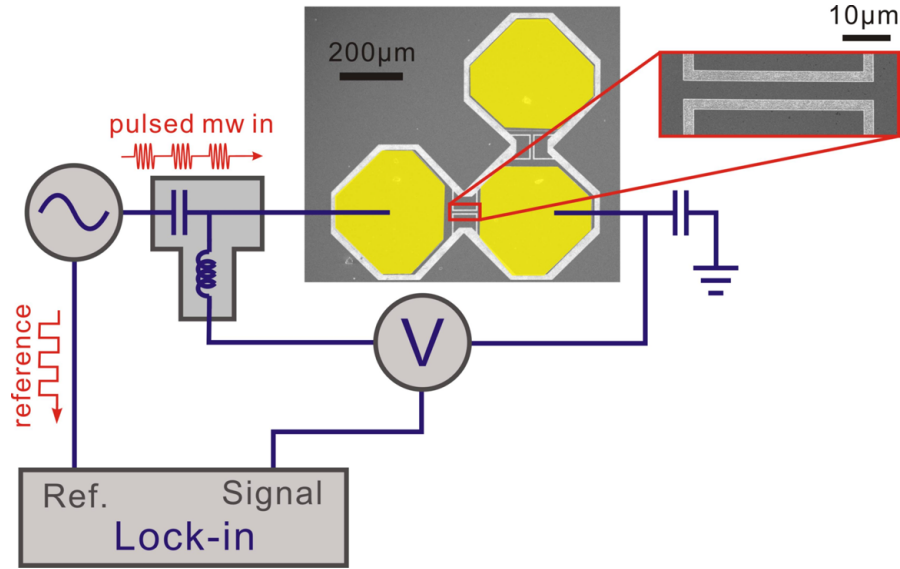

FIG. S8: Schematic of our SO-FMR setup. The main figure illustrates the lock-in measurement technique. SEM images: The sample consists of two micro-bars 90°-apart and along distinct crystalline axes. The Au/Cr ohmic contacts are highlighted with yellow false colours. The inset shows an enlarged SEM image on one of the micro-bars (4 μm-wide).

Using the four-band Kohn-Luttinger Hamiltonian model, the inversion symmetric part $\mathcal{H}_{\mathrm{KL}}$ is

$$\mathcal{H}_{\mathrm{KL}} = \frac{\hbar^2}{2m}\left[\left(\gamma_1 + \frac{5}{2}\gamma_2\right)k^2 - 2\gamma_3(\vec{k}\cdot\vec{J})^2 + 2(\gamma_3 - \gamma_2)\sum_i k_i^2 J_i^2\right] \tag{S26}$$

where [16] $\gamma_1 = 6.98$, $\gamma_2 = 2.06$, $\gamma_3 = 2.93$, $\vec{J}$ is the carrier total angular momentum and $\vec{k}$ is the wavevector. The
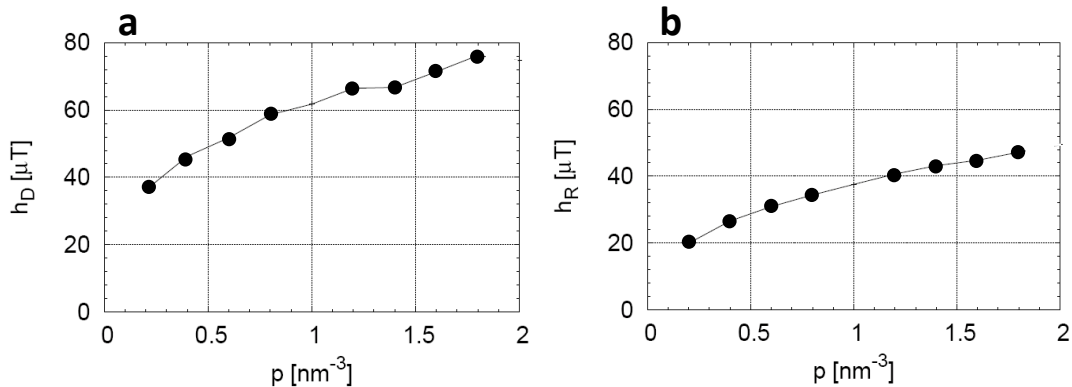
FIG. S9: Magnitude of the effective fields calculated from Eq. S29, using $\hbar/\tau = 100$ meV and $E = 10^3$ V/cm typical for our experiments. **a,** Dresselhaus symmetry contribution for $|e_0| = 0.1\%$. **b,** Rashba symmetry contribution for $|e_{xy}| = 0.1\%$.

hole–Mn exchange term reads:

$$\mathcal{H}_{\mathrm{exch}} = \frac{1}{3} h \mathbf{e}_M \cdot \vec{J} \tag{S27}$$

where [13] $h = J_{pd} N_{\mathrm{Mn}} S_{\mathrm{Mn}}$, N_{Mn} is the density of Mn local moments, $S_{\mathrm{Mn}} = 5/2$, and $\mathbf{e}_M$ is the magnetisation unit vector. Finally, the strain-induced term that breaks the inversion symmetry of $\mathcal{H}$ in Eq. (S25) is written as

$$\begin{aligned} \mathcal{H}_{\mathrm{C4}} &= C_4[J_x k_x (e_{yy} - e_{zz}) + J_y k_y (e_{zz} - e_{xx}) + J_z k_z (e_{xx} - e_{yy})] \\ &+ C_4[(J_x k_y - J_y k_x) e_{xy} + (J_y k_z - J_z k_y) e_{yz} + (J_z k_x - J_x k_z) e_{zx}] \end{aligned} \tag{S28}$$

which is identical to the expression quoted in the main text; $C_4 \approx 0.5$ eVnm for the GaAs host [12]. The $\mathbf{h}_{\mathrm{D}}$ and $\mathbf{h}_{\mathrm{R}}$ components of $\mathbf{h}_{\mathrm{eff}}$ originate from the first and second bracket term in the Hamiltonian (S28), respectively.

In the linear response regime of our experiments, the effective field is given by [14]:

$$\mathbf{h}_{\mathrm{eff}} = -\frac{eE J_{pd}}{\mu_B} \tau \int \frac{d^3 k}{(2\pi)^3} \sum_n \langle \mathbf{s} \rangle_{n,\mathbf{k}} \langle v_I \rangle_{n,\mathbf{k}} \delta(\varepsilon_{n,\mathbf{k}} - \varepsilon_F), \tag{S29}$$

where $\langle \mathbf{s} \rangle_{n,\mathbf{k}}$ denotes the expectation value of the carrier spin, $\langle v_I \rangle_{n,\mathbf{k}}$ the velocity component along the current direction, $\varepsilon_{n,\mathbf{k}}$ are the eigenenergies of the Hamiltonian $\mathcal{H}$, and ε_F is the Fermi energy. So $\mathbf{h}_{\mathrm{eff}}$ is proportional to the applied electric field E, to the hole–Mn exchange constant J_{pd} (≈ 55 meVnm^3 in (Ga,Mn)As [13]), to the transport relaxation time τ ($\hbar/\tau \approx 100$ meV [13]), and to the non-equilibrium spin-density due to the displaced Fermi surface as given by the integral in Eq. S29.

For evaluating the $\mathbf{h}_{\mathrm{D}}$ component of the current-induced effective field we assume only the growth strain to be present: $e_{xy} = 0$, $e_{xx} = e_{yy} = 0$ and $e_{zz} = -e_0$ (z is the growth direction). As mentioned in the main text, $\mathcal{H}_{C4}$ then assumes, up to the prefactor, the form of the Dresselhaus Hamiltonian known for 2D systems with bulk inversion asymmetry. The carrier density p and the local Mn moment density N_{Mn} are the other two input parameters of the calculation ($N_{\mathrm{Mn}} = 0.04x/a_{lc}^3$, where x is the doping in percent of uncompensated Mn$_{\mathrm{Ga}}$ local moments and a_{lc} is the lattice constant of the material). Having surveyed the range from 0.2 to 2.0 nm^{-3} for p and 2% to 10% for x, we conclude that: (i) For a fixed current direction $\mathbf{I}$, the effective field calculated from Eq. S29 depends moderately weakly on the magnetisation direction $\mathbf{e}_M$. (ii) The calculated $\mathbf{h}_{\mathrm{D}}$ has the Dresselhaus symmetry. (iii) The magnitude of $\mathbf{h}_{\mathrm{D}}$ is linearly proportional to the growth strain e_0 and depends only weakly on the direction of $\mathbf{I}$. (iv) $\mathbf{h}_{\mathrm{D}}$ depends only very weakly on x. (v) Finally, $\mathbf{h}_{\mathrm{D}}$ monotonically increases with increasing p, as shown in Figure S9a, but the dependence is relatively weak for $p = 0.5 - 1.5$ nm^{-3} relevant for our measured samples. For carrier density $p \approx 1$ nm^{-3} the calculated effective field at $E = 10^3$ Vcm^{-1} is $h_{\mathrm{D}} \approx 60$ μT which is consistent with our experimental values.

The Rashba component of the effective field, $\mathbf{h}_{\mathrm{R}}$, is calculated assuming $e_0 = 0$ and $e_{xy} \neq 0$. The results are analogous in all points listed above to the results for $\mathbf{h}_{\mathrm{D}}$. The carrier density dependence of $\mathbf{h}_{\mathrm{R}}$ is plotted in Figure S9b.

As mentioned above, $\mathbf{h}_{\mathrm{D}}$ originates from the diagonal strain term in the Hamiltonian (Eq. S28). In our samples the diagonal strain is produced by the lattice mismatch between the GaAs substrate and (Ga,Mn)As [17]. The off-diagonal strain component which yields the $\mathbf{h}_{\mathrm{R}}$ field is not physically present in the crystal structure of (Ga,Mn)As epilayers. It has been introduced, however, in previous studies to model the in-plane uniaxial anisotropy present

in (Ga,Mn)As and the fitted values of this effective off-diagonal strain are typically several times smaller than the diagonal, growth-induced strain [18]. This is consistent with the observed smaller magnitude of $\mathbf{h}_R$ than $\mathbf{h}_D$ in our measurements. We note that this arguably fictitious off-diagonal strain in the $\mathbf{k}\cdot\mathbf{p}$ Hamiltonian has an effect similar to a potential that breaks the symmetry between [110] and [$\bar{1}$10] crystallographic directions. In Appendix A of Ref. [18] it is for example shown how a potential $V(x,y,z) = \xi xy$ induces such corrections to the $\mathbf{k}\cdot\mathbf{p}$ Hamiltonian and how the strength of this symmetry-breaking ξ can in principle be linked to the off-diagonal strain e_{xy}^{int}.

The $\mathcal{H}_{C4}$ origin of the effective field is confirmed with the measurements on 500 nm-wide bars patterned on the $(Ga_{0.94},Mn_{0.06})(As_{0.9},P_{0.1})$ epilayer (Figure 3d & f in the main text), which has an opposite sign of the growth-strain than the $(Ga_{0.94},Mn_{0.06})As$ film [19]. Consistently, the observed field $\mathbf{h}_D$ also changes sign. Apart from this sign change we also observe a larger magnitude of $\mathbf{h}_D$ at a given current density in the (Ga,Mn)(As,P) epilayer. This could be due to the larger magnitude of the growth-strain and larger resistivity (larger E at given j) of (Ga,Mn)(As,P) as compared to the (Ga,Mn)As film [19].

---

[1] Rushforth, A., Výborný, K., King, C. S., Edmonds, K., Campion, R. P., Foxon, C. T., Wunderlich, J., Irvine, A. C., Vašek, P., Novák, V., Olejník, K., Sinova, J., Jungwirth, T., and Gallagher, B. L. *Phys. Rev. Lett.* **99**, 147207 (2007).

[2] Heinrich, B. and Cochran, J. F. *Adv. Phys.* **42**, 523–639 (1993).

[3] Mecking, N., Gui, Y. S., and Hu, C.-M. *Phys. Rev. B* **76**, 224430 (2007).

[4] Aharoni, A. *J. Appl. Phys* **83**, 3432 (1998).

[5] Counil, G., Kim, J.-V., Devolder, T., Chappert, C., Shigeto, K., and Otani, Y. *J. Appl. Phys* **94**, 5646 (2004).

[6] Liu, X. and Furdyna, J. K. *J. Phys.: Condens. Matter* **18**, R245 (2006).

[7] Yamaguchi, A., Motoi, K., Hirohata, A., Miyajima, H., Miyashita, Y., and Sanada, Y. *Phys. Rev. B* **78**, 104401 (2008).

[8] Thiaville, A. and Nakatani, Y. *J. Appl. Phys* **104**, 093701 (2008).

[9] Costache, M. V., Watts, S. M., Sladkov, M., van der Wal, C. H., and van Wees, B. J. *Appl. Phys. Lett.* **89**, 232115 (2006).

[10] Costache, M. V., Sladkov, M., van der Wal, C. H., and van Wees, B. J. *Appl. Phys. Lett.* **89**, 192506 (2006).

[11] Bir, G. L. and Pikus, G. E. *Symmetry and strain-induced effects in semiconductors.* Wiley in New York, (1974).

[12] Silver, M., Batty, W., Ghiti, A., and O'Reilly, E. P. *Phys. Rev. B* **46**, 6781 (1992).

[13] Jungwirth, T., Sinova, J., Mašek, J., Kučera, J., and MacDonald, A. H. *Rev. Mod. Phys.* **78**, 809–864 (2006).

[14] Garate, I. and MacDonald, A. H. *Phys. Rev. B* **88**, 134403 (2009).

[15] Chernyshov, A., Overby, M., Liu, X., Furdyna, J. K., Lyanda-Geller, Y., and Rokhinson, L. P. *Nature Phys.* **5**, 656–659 (2009).

[16] Vurgaftman, I., Meyer, J. R., and Ram-Mohan, L. R. *J. Appl. Phys.* **89**, 5815–5875 (2001).

[17] Ohno, H. *Science* **281**, 951–956 (1998).

[18] Zemen, J., Kučera, J., Olejník, K., and Jungwirth, T. *Phys. Rev. B* **80**, 155203 (2009).

[19] Rushforth, A. W., Wang, M., Farley, N. R. S., Campion, R. P., Edmonds, K. W., Staddon, C. R., Foxon, C. T., and Gallagher, B. L. *J. Appl. Phys.* **104**, 073908 (2008).